Wiley
International Journal of Energy Research
Volume 2025, Article ID 9267226, 16 pages
https://doi.org/10.1155/er/9267226

WILEY

Research Article

Intelligent Decision Supporting System for Precursors of Rock Instability: The Application of Early Warning of Rock Shear-Slip Instability

Xun You[1,2] **Yunmin Wang**[1,3] **Xiangxin Liu**[3,4] **Kui Zhao**[1] **Bin Gong**[5] **and Xianxian Liu**[4]

[1]*School of Resource and Environmental Engineering, Jiangxi University of Science and Technology, Ganzhou 341000, China*
[2]*Baowu Resources Corporation Limited, Shanghai 200126, China*
[3]*State Key Laboratory of Safety and Health for Metal Mines, Maanshan 243000, China*
[4]*School of Civil and Surveying and Mapping Engineering, Jiangxi University of Science and Technology, Ganzhou 341000, China*
[5]*Department of Civil and Environmental Engineering, Brunel University London, London, UB8 3PH, UK*

Correspondence should be addressed to Xiangxin Liu; liuxx@jxust.edu.cn

Received 12 April 2025; Revised 10 June 2025; Accepted 15 July 2025

Academic Editor: Meilu Yu

Underground mining is developing towards deep and large scales; the safety production situation of mining becomes more and more severe. The difficulty of early warning of rock mass instability has increased sharply. The rock shear-slip test is carried out first, crack propagation features are investigated. Based on the idea of “the integrated development of deep learning technology and mine rock mass monitoring,” an intelligent decision-making platform (IDMP) for the precursors of rock instability is proposed. The results show that the crack network of marble specimens under the shear-slip test is composed of dominant and secondary cracks. The intelligent identification model (IIM) of rock shear slip instability is constructed by the long short-term memory network (LSTM), with 16 kinds of acoustic emission (AE) timing parameters as the input vectors and three states of no warning [0, 0], first-level warning [1, 0], and second-level warning [1, 1] as the output ends. The instability IIM can effectively identify rock shear-slip instability and determine the early warning level, and the recognition effect is good. Finally, based on the IIM, an IDMP for rock instability precursors is constructed. IDMP consists of an early warning identification layer, an early warning analysis layer, and an early warning decision-making layer, which can make intelligent decisions on whether to give early warning and determine the level of early warning. The research results provide a new idea and method for the intelligent identification and early warning release of rock mass instability early warning information.

Keywords: intelligent decision-making platform (IDMP); intelligent identification model (IIM); mining practice; precursors of rock instability; rock mechanics

Summary

- Intelligent Decision-Making Platform (IDMP) for rock instability precursors is constructed based on the Intelligent Identification Model (IIM).
- IDMP is composed of an early warning identification layer, an early warning analysis layer, and an early warning decision-making layer, which makes the intelligent decisions about the different kinds of warning levels.

1. Introduction

Large-scale underground mining sites have caused great stress perturbations to the underground rock mass. It is essential to

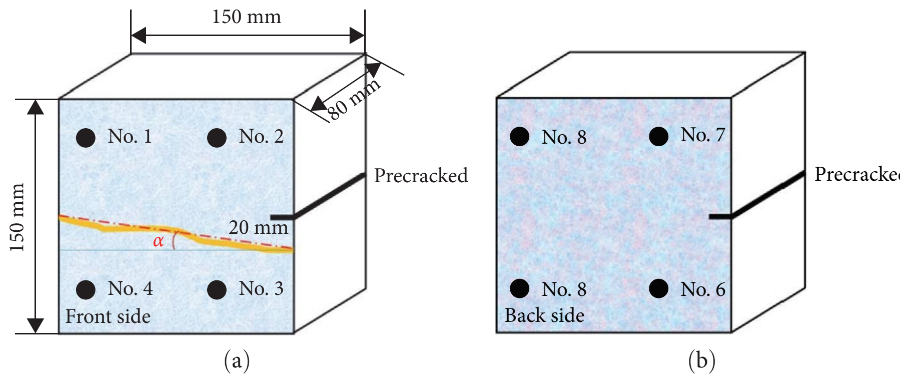

FIGURE 1: The size of marble specimens. (a) front, (b) back.

carry out the research on the real-time monitoring of rock mass and the early warning of its instability [1–3]. The early warning of rock mass failure is extremely important and also a significant challenge in the engineering and academic worlds [4–6].

Neural networks (NNs) have been used widely in the fields of stability monitoring and early warning of rock mass. An image identification model based on convolutional NN was established for the seismic waveforms of microseismic (MS) events and blasts, the accuracies of MS events and blasts reached 99.46% and 99.33% [7]. Wu et al. [8] constructed a rockburst intensity classification prediction model based on the principal component analysis-probabilistic neural network (PCA-PNN) principle, and verified that its prediction performance was superior to the support vector machine (SVM) model and artificial neural network (ANN) model, with faster convergence speed. Wu et al. [9] combined synthetic minority oversampling technique (SMOTE) and convolutional neural networks (CNNs) for landslide susceptibility assessment, reaching 89.50% model accuracy. Tian et al. [10] developed a rockburst prediction model based on a deep neural network (DNN) incorporating Dropout and an improved Adam algorithm (DA-DNN), achieving 98.3% accuracy with 289 engineering case studies. Cusp mutation theory used to be a new integrated model for rock instability prediction and early warning, this kind of warning model performed better [11]. Feng et al. [12] reviewed the recent achievements made by our team in the mitigation of rockburst risk, included the application of NN modeling and the establishment of a quantitative warning method. Wang [13] used the quiet period of AE and MS events to be an early warning key point. Zhang et al. [14] adopted CNN-LSTM model for regression prediction of rock mass deformation and risk warning classification. Wang et al. [15] adopt the back propagation neural network (BPNN) prediction model to provide a basis for safely and efficiently predicting coal mine disasters, and it obtained a good predictive performance. Huang et al. [16, 17] reviewed several important uncertain issues of landslide susceptibility prediction (LSP), and innovatively constructed the semi-supervised imbalanced theory for reasonable LSP modeling. Ma et al. [18] proposed a MS-based method and its implementation steps for numerical simulation and the interpretation of hard rock fracture. Li et al. [19] effectively proposed a novel hazard classification safety warning strategy for battery failure. Mao et al. [20] developed efficient reduced-order models (ROMs) for Underground hydrogen (H_2) storage (UHS) in depleted natural gas reservoirs using DNNs based on comprehensive reservoir simulation data sets.

Preliminary research has accumulated a lot of results, including algorithms optimization, computational efficiency, algorithm redundancy, and so on. However, the influencing factors of rock mass stability are extremely complex. The selection of precursor early warning parameters depends on experience, and the monitoring accuracy and early warning accuracy are still not guaranteed.

In this research, the rock shear-slip fracturing test is carried out by acoustic emission (AE) monitoring. With the guiding ideology of "integrated development of deep learning technology and rock mass monitoring," an intelligent decision-making platform (IDMP) for rock instability precursors is constructed. The digital level of monitoring is continuously improved, so as to provide a solution to the difficulty of monitoring and early warning.

2. Rock Shear Slip Test Scheme

2.1. Rock Specimen. The size of marble specimen is 150 mm × 150 mm × 80 mm^3, and pre-cracked in 20 mm length is set at the position of 75 mm on site, which is parallel to the direction of shear load (Figure 1). Marble specimen with obvious natural bedding structure is selected, the bedding dip α (Figure 1) is 0° (Figure 2a), 20° (Figure 2b), 30° (Figure 2c), 60° (Figure 2d).

Marble specimen named is set as the forms of MRS-XX. MRS means "marble shear-slip". XX means "bedding dip α", MRS-00 is marble specimen in the dip 0°, MRS-20 is marble specimen in the dip 20°, MRS-30 is marble specimen in the dip 30°, and MRS-60 is marble specimen in the dip 60°.

2.2. Test Equipments. Testing system is shown in Figure 3, which is composed of a horizontal loading unit, a vertical loading unit, a measurement control unit, etc. Testing system (RLW-3000) is used here, which can provide a maximum axial force of 3000 kN and a maximum shear force of 1000 kN. AE monitoring system (PCI-Express) produced by PAC in the United States is chosen, and eight number of sensors are utilized (Figure 2b). It is necessary to ensure that the data of the loading equipment and the monitoring equipment are strictly corresponded to the time, and the timing of each equipments is synchronized.

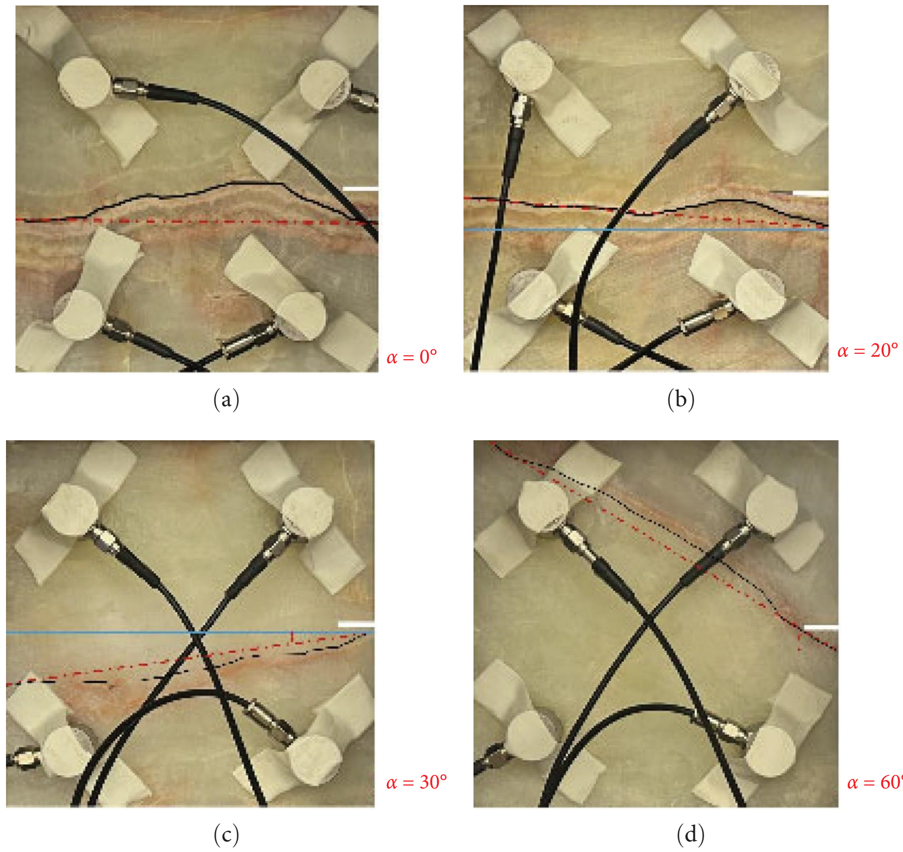

FIGURE 2: Marble specimens with different bedding dips. (a) MRS-00, (b) MRS-20, (c) MRS-30, and (d) MRS-60.

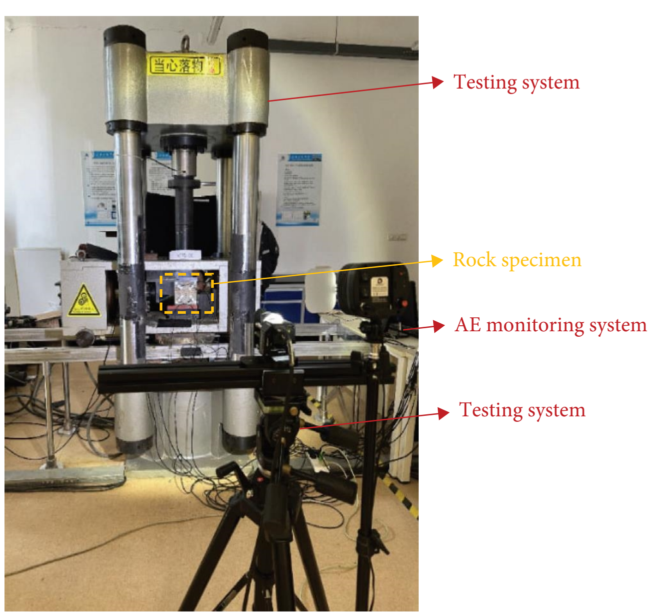

FIGURE 3: Testing setup. Testing site and AE sensors arrangement.

All rocks adopt the same equipment parameter settings as following: (1) AE monitoring system, eight models of Nano-30 sensors are symmetrically arranged on the front and back sides of the specimen, the sampling rate is 1MSPS, the threshold value is 45 dB, and the preamplifier gain is 30dB; (2) HD camera, sampling frequency is 2 frames/s.

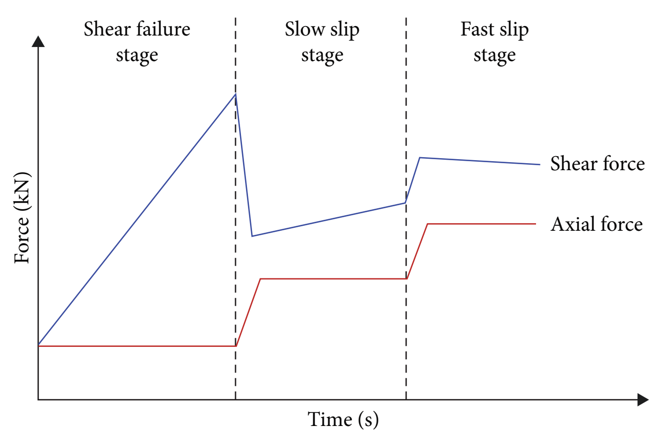

FIGURE 4: Schematic diagram of normal and shear loading paths.

2.3. Loading Path. Go enhance the comparability of the monitoring results of rock shear slip tests under different lithologies and different bedding dips, same loading path is used for all experiments in this study (Figure 4).

1. Shear failure stage: after the axial and shear loads are preloaded to 50 kN. After the axial direction is loaded at 500 N/s to 100 kN, the axial direction is set to a fixed

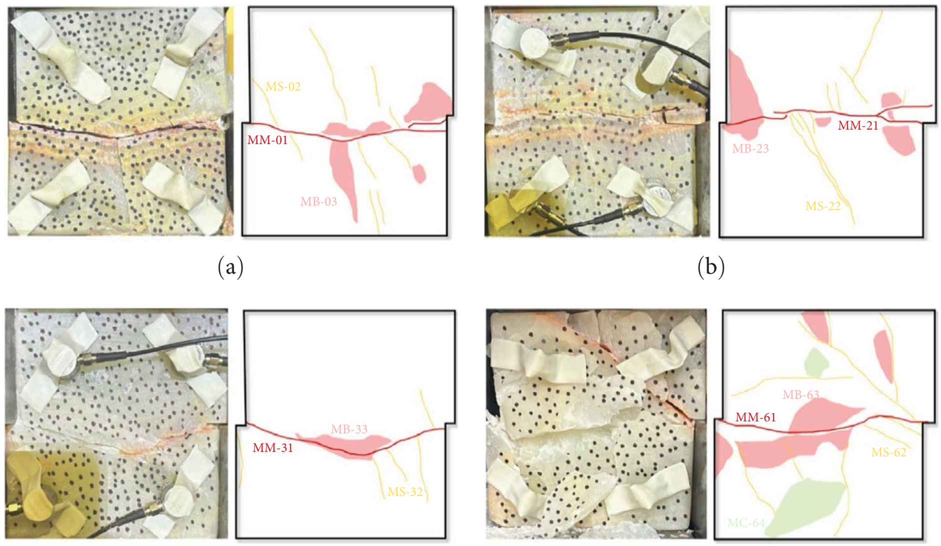

(a) (b) (c) (d)

FIGURE 5: Actual photos of shear-slip final fracture characteristics of rocks at different bedding dips. (a) MRS-00, (b) MRS-20, (c) MRS-30, and (d) MRS-60.

boundary. The shear direction is loaded at 0.15 mm/min until the shear failure occurs, and the maximum load is reached in the shear direction.

2. Slow slip stage: After the axial direction is increased from 500 N/s to 200 kN, the axial direction is set to a fixed boundary. The shear direction slips 1.5 mm at the rate of 0.12 mm/min.
3. Fast slip stage: After the axial direction is increased from 500 N/s to 300 kN, the axial direction is set to a fixed boundary. The shear direction slips 1.5 mm at the rate of 0.3 mm/min.
4. The end: Store test data and clean up the test site.

2.4. Test Results

2.4.1. Analysis of Final Failure Characteristics. With the same loading path (Figure 4), final failure patterns of different bedding marble specimens have the same place (Figure 5). Dominant cracks (MM-01, Figure 5a; MM-21, Figure 5b; MM-31, Figure 5c; MM-61, Figure 5d) divide rock specimen into upper and lower blocks, and dominant cracks are mainly coalesced along the pre-cracked. Secondary cracks are shown in (MS-02, Figure 5a; MS-22, Figure 5b; MS-32, Figure 5c; MS-62, Figure 5d). Rocks have obvious rock detachment, exposing the inner rock area (MB-03, Figure 5a; MB-23, Figure 5b; MB-33, Figure 5c; MB-63, Figure 5d). The surface of MRS-60 specimen also captures the spalling phenomenon (MC-64, Figure 5d).

2.4.2. Analysis of Fracture Propagation. Figure 6 counts crack morphology of marble specimens at different stages with different dips. Solid dark red lines indicate dominant crack, solid orange lines indicate secondary crack, and pale red shaded areas indicate areas of fragmentation formed after the rock flakes are spalled or debris falls. The law of fracture propagation at each stage is summarized as follows:

- Marble MRS-00 specimen (Figure 6a): In the shear failure stage (Figure 6a, left), the penetrating dominant crack has been formed, the opening degree is not large, and the consistency with the bedding trend is good, and the rock is divided into upper and lower rock blocks. Two secondary cracks appear in the lower half of the rock. In the slow slip stage (Figure 6a, middle), the through-type dominant crack opens, and the staggered momentum of the upper and lower rock blocks along the dominant crack increases. Secondary cracks are distributed above and below the dominant cracks, and rock spalling appears in the middle of the right side. In the rapid slip stage (Figure 6a on the right), the opening of the penetrating dominant crack further increases, and the sliding dislocation momentum of the upper and lower rock blocks increases. The secondary crack continues to expand, and the fracture network formed becomes more complex.
- Marble MRS-20 specimen (Figure 6b): In the shear failure stage (Figure 6b, left), a penetrating dominant crack is formed along the bedding, and the dominant crack does not penetrate at the preset fracture. Secondary cracks are more developed than those of MRS-00. In the slow-slip stage (Figure 6b), the opening of dominant cracks further increases and the number of secondary cracks increases. A large area of rock blocks in the middle of the left side is spalled, and dominant cracks and preset cracks are connected by vertical fractures. In the rapid slip phase (Figure 6b, right), dominant cracks continued to open and the number of secondary cracks increase. The spalling area of the rock block in the middle of the left side is enlarged, and the spalling area is also formed in the vertical crack on the right.
- Marble MRS-30 specimen (Figure 6c): In the shear failure stage (Figure 6c, left), penetrating dominant cracks

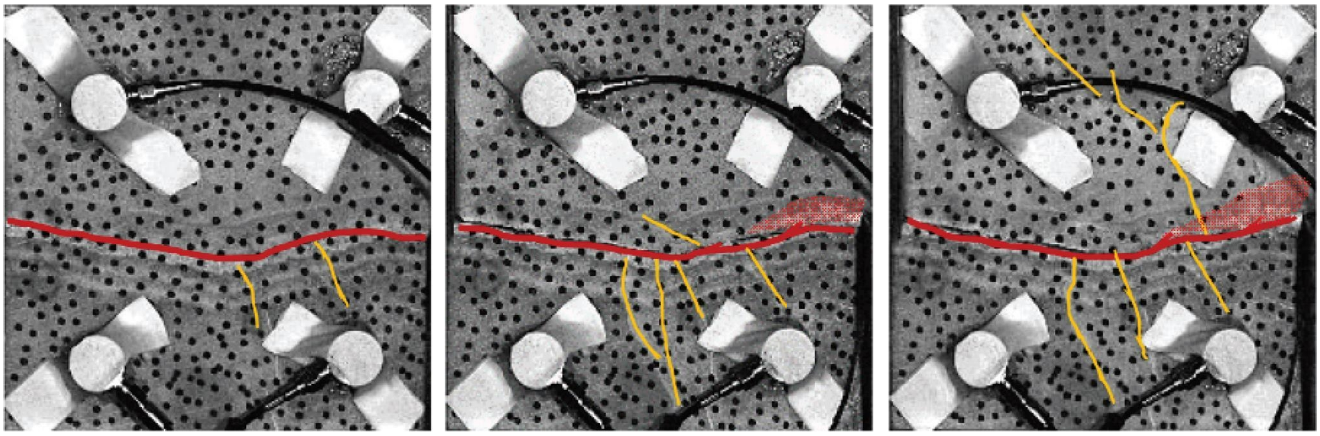

(a)

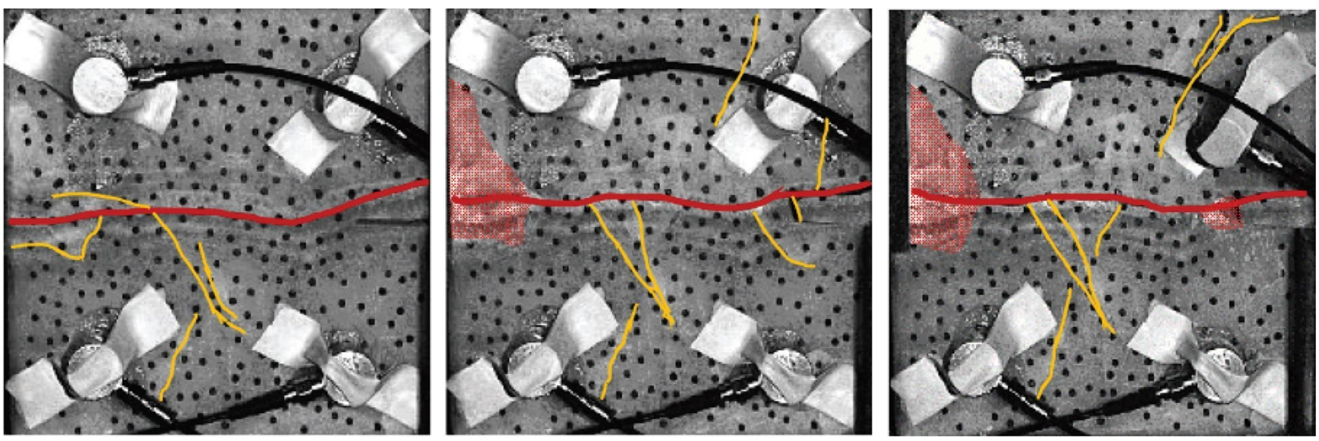

(b)

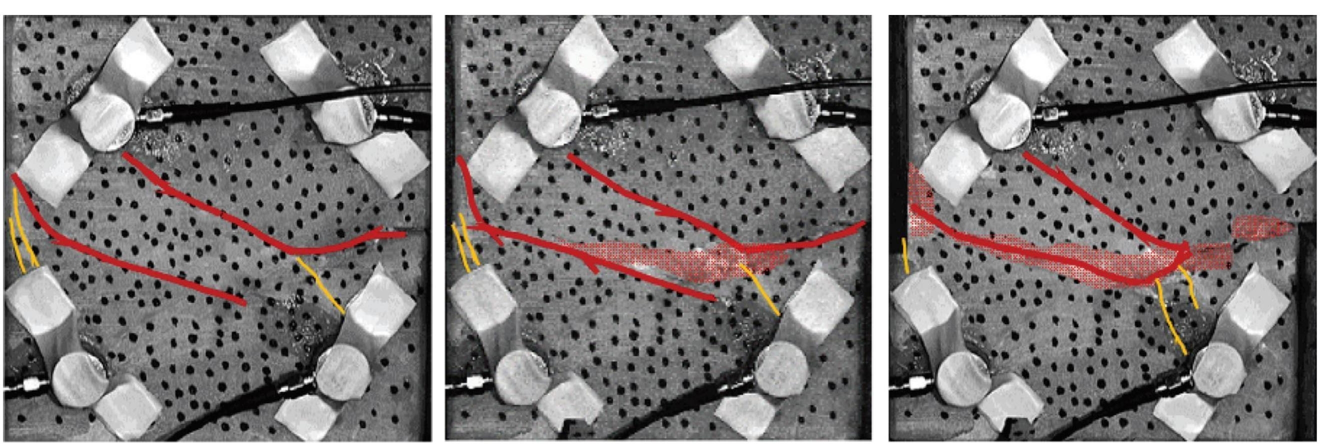

(c)

Figure 6: Continued.

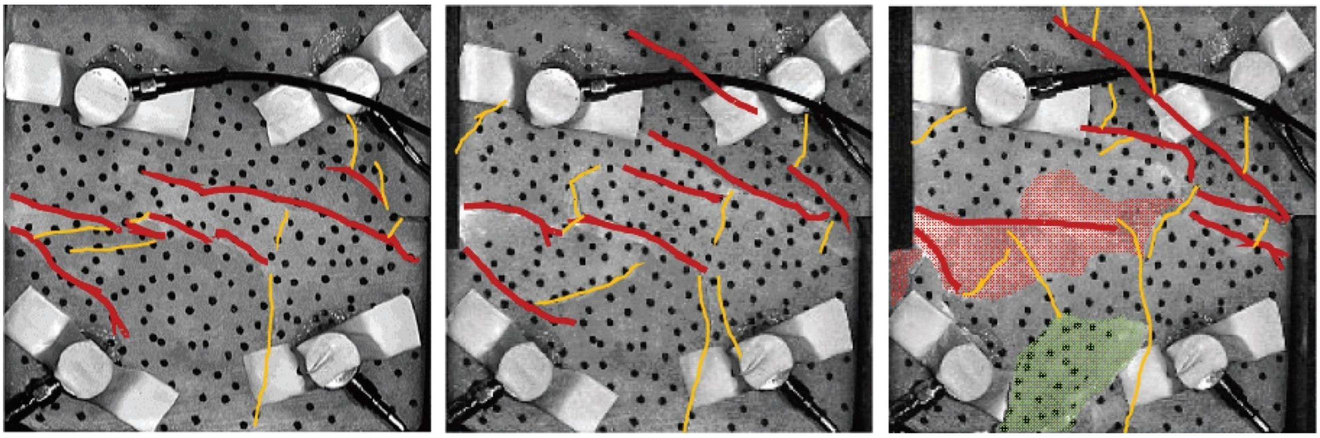

(d)

Figure 6: Actual photos of shear slip process of rocks at different bedding dips (from left to right, shear failure stage, slow slip stage, and fast slip stage). (a) MRS-00, (b) MRS-20, (c) MRS-30, and (d) MRS-60.

are not formed, but two dominant cracks that are nearly parallel along the bedding dip. Secondary cracks do not have MRS-00 and MRS-20 development. In the slow slip stage (Figure 6c, middle), the opening of the dominant crack does not increase, and a banded rock spalling area appears in the middle of the two dominant cracks. In the rapid slip stage (Figure 6c, right), two dominant cracks are connected in the striped rock spalling area, and the preset fractures in the middle of the left and the middle of the right are spalled in a small area.

- Marble MRS-60 specimen (Figure 6d): Fracture propagation is most affected by the rock bedding, and multiple dominant fractures are developed at the same dip as the shear direction. In the shear failure stage (Figure 6d, left), non-penetrating dominant cracks develop, and secondary cracks are distributed around the dominant cracks. In the slow slip stage (Figure 6d), the nonpenetrating dominant crack expands further, and secondary crack expands along the dominant crack. Dominant cracks are penetrated by secondary crack. In the rapid slip stage (Figure 6d right), dominant crack in the left middle spalls off after penetration, and the secondary crack continues to develop. Large rock chips that has fallen after peeling appear in the lower part.

There are similar rules for crack propagation in marble specimens with different bedding dips at different stages. Under the condition of shear-slip loading, one or more dominant fractures arranged in the same direction and multiple secondary fractures distributed near the dominant fractures are formed in marble specimens. As the loading progresses, the fracture state is closely related to the fracture at previous moment, that is, the fracture propagation follows the law of "inheritance". A number of dominant fractures arranged in the same direction are distributed in a goose-shaped manner, and the secondary fracture arrangement have a pinnate distribution pattern; that is, the crack distribution law of "the whole size of en echelon crack and the local region of pinnate crack" in terms of spatial–temporal aspects [21].

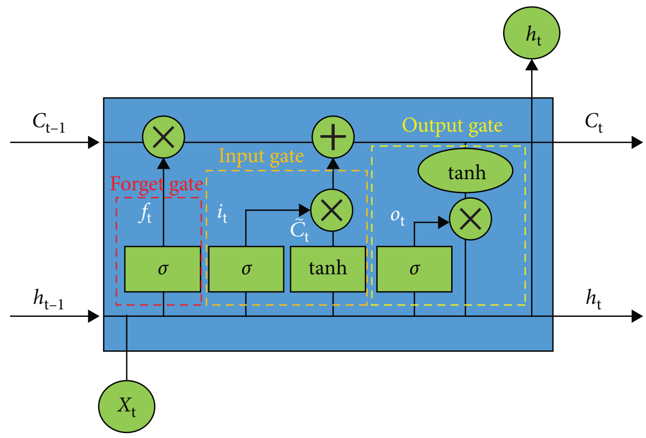

Figure 7: The schematic of LSTM structure.

3. Intelligent Identification of Rock Instability Based on LSTM

3.1. Introduction to LSTM. Long Short-Term Memory Network (LSTM) is a special type of Recurrent Neural Network (RNN), which is commonly used to deal with long-term dependency problems [22–24]. The LSTM consists of an input gate, a forget gate, an output gate, and a memory cell (Figure 7). The memory unit is used to save and update long-term dependent information throughout the sequence processing process. The input gate is used to decide which information to store in the memory cell. The forget gate is used to decide what information should be removed from the memory unit. The output gate is used to decide which information will be output to the next time step. Each gate uses a sigmoid activation function to determine the flow of information.

LSTM overcomes the gradient vanishing and gradient explosion problems of traditional RNNs in long sequence learning. LSTM is of high flexibility. LSTM can process input series of different lengths, which has been widely used in various fields, such as financial market forecasting, meteorological forecasting, earthquake prediction, and other time series forecasting.

Rise time	Count	Energy	Duration	Amplitude	Average frequency	RMS	ASL	Peak frequency	Threshold	Back-calculated frequency	Initial frequency	Signal intensity	Absolute energy	Center frequency	Peak frequency
202	191	61	2256	59	85	0.0014	27	30	45	78	148	385346	12499	241	261
39	54	19	1267	54	43	0.0008	21	4	45	40	102	122747	1957	176	95
154	40	15	1139	54	35	0.0008	21	9	45	31	58	94086	1347	199	94
247	25	8	570	50	44	0.0008	22	16	45	27	64	52054	768.271	199	94
271	50	20	1267	54	39	0.001	23	19	45	31	70	128292	2243	163	101
128	87	29	1703	55	51	0.0008	22	9	45	49	70	184193	3422	171	96
129	37	15	1117	50	33	0.0008	21	5	45	32	38	95788	1344	164	94
293	98	29	1855	54	53	0.0008	21	17	45	51	58	183491	3088	191	101
264	21	5	305	50	69	0.001	23	19	45	48	71	33327	561.992	188	96
44	17	7	578	50	29	0.0008	21	5	45	22	113	44286	573.346	172	102
57	16	7	632	50	25	0.0008	22	4	45	20	70	48327	615.062	153	95
145	41	13	824	52	50	0.0008	21	12	45	42	82	82722	1344	183	96
324	28	10	766	51	37	0.0008	22	16	45	27	49	66222	939.841	166	97
423	124	44	1839	58	67	0.0016	27	42	45	57	99	277590	7654	174	95
447	185	113	3822	65	48	0.0014	26	42	45	42	93	709018	28678	139	97
83	57	17	1050	53	54	0.0008	22	6	45	52	72	106259	1850	201	100
30	25	11	964	50	26	0.001	24	3	45	23	100	73112	943.26	160	97
60	21	11	900	51	23	0.0012	25	5	45	19	83	71141	923.238	122	102
42	87	32	1648	56	53	0.0012	25	5	45	51	119	202917	4413	139	98

FIGURE 8: Feature dataset of learning samples.

TABLE 1: Statistical table of rock specimens.

Specimen number	Instability time t_w (s)	Data of input layer /group	Data of output layer								
			No warning [0,0] /group	Level 1 warning [1,0]				Level 2 warning [1]			
				Number /group	Start of early warning t_1 (s)	Duration of warning ΔT_1	Lead rate of early warning K_1	Number /group	Start of early warning t_2 (s)	Duration of warning ΔT_2	Lead rate of early warning K_2
MRS00-1	1011.29	210,202	189,603	14,357	596.47	125.2	58.98	6242	978.21	11.98	96.73
MRS20-1	1149.09	204,709	204,157	385	527.12	346.15	45.87	167	1089.55	13.19	94.82
MRS30-1	1291.79	277,469	277,213	208	718.57	164.34	55.63	48	1116.70	12.52	86.45
MRS60-1	2213.55	259,234	257,631	1210	1846.40	143.71	83.41	393	2165.75	24.81	97.84

Note: $K_1 = \frac{t_1}{t_w} \times 100\%$, $K_2 = \frac{t_2}{t_w} \times 100\%$.

3.2. IIM Construction Based on LSTM

3.2.1. Learning Samples. Since the discovery of the Kaiser effect in the 1950s, AE technology has gradually become an important tool in the field of nondestructive monitoring. Goodman experimentally confirmed that rocks also exhibit the Kaiser effect [25], which laid the theoretical foundation for the further development of AE technology in geotechnical mechanics. The role of AE signals in analyzing the fracture process of rocks under stress has been widely studied [26–29]. During the stress process, the propagation and rupture of microcracks generate AE signals, the characteristics of which are closely related to the rock's instability process. For instance, higher-frequency AE signals typically reflect the early stages of crack propagation, while during the instability process, both the frequency and amplitude of the signals may change. By analyzing these AE signals, it is possible to identify the instability state of the rock, thereby providing early warning information.

Learning samples are related to the redundancy of the input vectors of the model, which is an important part of improving the recognition accuracy and optimizing the learning performance of the NN. Rock fracture AE data has a large short-term volume, a vast amount of information and high dimensionality, which is exactly aligned with the concept of big data (Appendix Tables A1–A4). According to the AE timing information obtained from the experiment (Figure 8), there are 16 eigenvectors, including rise time, count, energy, duration, amplitude, average frequency, RMS, ASL, peak frequency, threshold, back-calculated frequency, initial frequency, signal intensity, absolute energy, center frequency, and peak frequency. The learning sample is composed of these 16 eigenvectors.

The IIM proposed in this paper is based on the concept of big data, which no longer cleans the data, and uses all the collected effective feature information for the input layer feature vector.

3.2.2. Model Construction. The input vector is composed of 16 parameters of rock failure AE timing (Figure 8), and there are three states of the output vector, namely, no warning, first-level warning, and second-level warning. Suppose "00" does not give an early warning, "10" gives a first-level warning, and "11" gives a second-level warning. The input vector consists of 16 AE timing parameters normalized (rise time, count, energy, duration, amplitude, average frequency, RMS, ASL, peak frequency, threshold, back-calculated frequency, initial frequency, signal strength, absolute energy, center frequency, peak frequency). The output vector is represented by [00,10,11].

3.2.3. Model Training. The dataset (Table 1) is divided into a training set (Table 2) and a test set (Table 3). The training set is used for model training, and the test set is used to evaluate the performance of the model. The initial learning rate of the training is set to 1×10^{-4}, the training batch size is set to 32, the total number of training rounds is set to 100 epochs, the loss

Table 2: Model training statistics.

Filename	Enter layer data/group	Output layer data			Training data		
		No warning [0,0] /group	Level 1 early warning [1,0]/group	Level 2 early warning [1]/group	Loss function	Training duration (s)	Loss curve convergence
Train.xlsx	862,502	845,534	11,931	5037	Binary cross-entropy loss function	1668	Convergence

Table 3: Model test statistics.

Filename	Enter layer data/group	Output layer data			Evaluation indicators	
		No warning [0,0] /group	Level 1 early warning [1,0]/group	Level 2 early warning [1]/group	MAE	RMSE
Text.xlsx	89,112	83,070	4229	1813	0.08	0.19

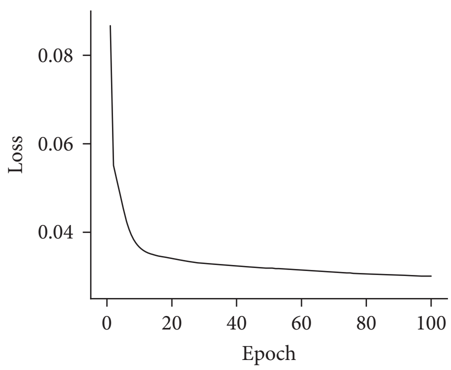

Figure 9: The variation of Loss with Epoch.

function is Binary Cross-Entropy Loss (BCE Loss), and the optimizer is Adam optimizer, so that the model can dynamically adjust the learning rate to optimize the training effect. Lead rate of early warning (K) represents the percentage of start of early warning time relative to the instability time, reflecting the system's capability to provide prewarning duration for preventing property loss and ensuring safety. Analyzing the training effect from the values of the loss function, the loss function value decreases as the number of epochs increases (Figure 9). Finally, it tends to stabilize and converge, which indicates the effectiveness of the training.

3.3. IIM of Rock Shear-Slip Instability Based on LSTM. Mean absolute error (MAE) and root mean square error (RMSE) are selected to evaluate the performance of the model as the evaluation indexes [30]. MAE is the average value of the absolute error between the predicted value and the true value (Equation (1)). It provides a direct measure of the average magnitude of errors in the model's predictions, without considering the direction of the error. A lower MAE indicates better performance, reflecting fewer discrepancies between predicted and true values. RMSE is the square root of the average of all errors squared (Equation (2)). RMSE gives more weight to larger errors due to the squaring of the differences, making it sensitive to outliers. A lower RMSE suggests that the model's predictions are more accurate overall, particularly in terms of handling larger deviations from the true values. Both MAE and RMSE are important for understanding different aspects of model performance. While MAE is more straightforward and interprets the error as an average, RMSE highlights the significance of larger errors. Together, these indices provide a comprehensive view of the model's performance. The closer the evaluation index value is to 0, the better the model performance.

$$\mathrm{MAE} = \frac{1}{n}\sum_{i=0}^{n} \left| \widehat{y}_i - y_i \right|, \tag{1}$$

$$\mathrm{RMSE} = \sqrt{\frac{1}{n}\sum_{i=0}^{n} \left(\widehat{y}_i - y_i \right)^2}, \tag{2}$$

where n is the number of samples, $\widehat{y}_i$ is the predicted value, y_i is the true value.

Table 4 shows that the constructed intelligent early warning information identification model can effectively identify the rock shear slip instability and determine the early warning level by the collected rock AE time series information, and the recognition effect is good.

4. IDMP for the Precursors of Rock Instability

The effective security early warning and the alarm technology provide comprehensive information, such as the security levels, violation components, and the security trend of the system before a fault occurs [21, 31]. Figure 10 is a schematic diagram of the rock instability precursor IDMP, which is mainly used for intelligent early warning identification and early warning decision-making of instability information, and the platform comprises three modules, namely early warning identification layer, early warning analysis layer and early warning decision-making layer.

TABLE 4: Statistics of intelligent identification results.

Specimen number	Instability time t_w (s)	Data of input layer /group	Output layer data								
			No warning [0,0] /group	Level 1 early warning [1,0]/group				Level 2 early warning [1]/group			
				Number /group	Start of early warning t_1 /s	Duration of warning ΔT_1	Lead rate of early warning K_1	Number /group	Start of early warning t_2 (s)	Duration of warning ΔT_2	Lead rate of early warning K_2
RSLT-1	1108.51	79,105	77,317	1768	462.89	79.82	41.76	20	1048.12	10.67	94.55
RSLT-3	1092.26	2777	2584	180	632.91	134.54	57.94	13	999.65	20.19	91.52
RSLT-4	1121.34	36,316	36,189	113	702.26	100.74	62.63	14	1000.12	29.25	89.19
RSLT-5	990.93	39,120	38,447	662	589.54	176.67	59.49	11	950.76	15.23	95.95

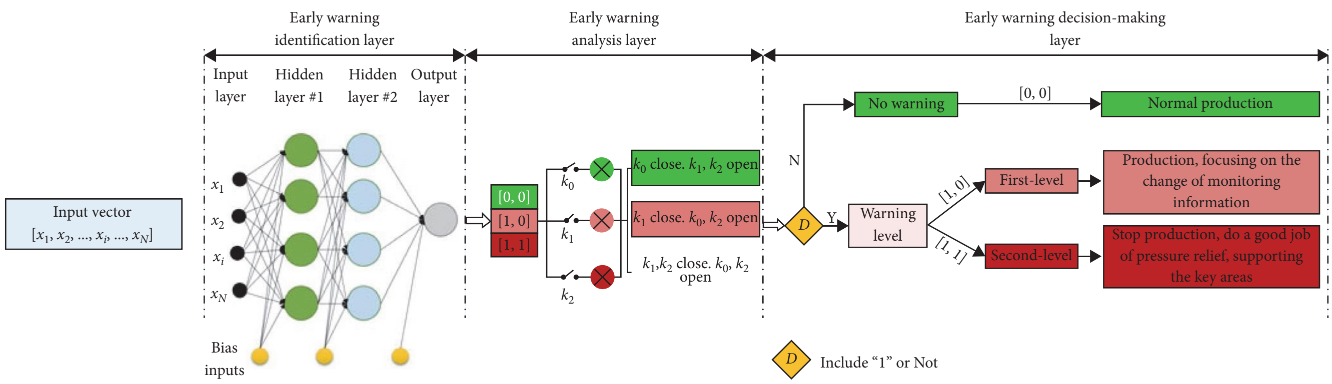

FIGURE 10: Intelligent decision-making platform for rock instability precursors.

- Early warning identification layer: The input vector of LSTM is formed after the normalized processing of the collected monitoring information, that is intelligent identification layer of early warning information. According to the idea of big data, the input layer directly normalizes the collected monitoring information to form the input vector of LSTM $[x_1, x_2, \ldots, x_i, \ldots x_N]$, and no longer selects feature data. The IIM is constructed through the LSTM NN, and the recognition accuracy and efficiency of the model are optimized from multiple perspectives, and the output is a representation vector containing early warning information [0,0,1,0] and [1].
- Early warning analysis layer: Based on the early warning identification results, the analysis line is designed to provide early warning information for the early warning decision-making layer. When output [0,0], $k_0$close, k_1、 k_2 open, green light on. When output [1,0],k_1 closed, k_0、 k_2 is open, a red light is on, that is level 1warning. When output [1], k_1、 k_2 is closed, k_2 is open, two red lights are on, that is level 2 warning.
- Early warning decision-making layer: Based on the output results of the line analyzed by the early warning analysis layer, the early warning level is determined by the decision-maker D. If the output result does not have 1, no warning will be given, and the decision will be 'normal production'. When output is 1, enter the early warning mode, [1, 0] is the first level of early warning, and the decision is 'production, focusing on the change of monitoring information'; [1, 1] is a second-level early warning, and the decision is to 'stop production, do a good job of pressure relief, supporting the key areas'.

Through the whole process of "Early warning identification layer → Early warning analysis layer → Early warning decision-making layer", the IDMP for rock instability precursors constructed in Figure 10 is used to intelligently identify the AE timing information of rock specimens RSLT-1, RSLT-3, RSLT-4 and RSLT-5, which is effectively used for the intelligent identification of rock instability precursor information. This platform can be practically applied in various scenarios, such as monitoring rock instability in mining operations, providing early warnings in underground tunnel construction to prevent accidents, and supporting geotechnical engineers in evaluating potential landslides or rockfalls in mountainous regions. The intelligent identification of rock instability precursor information plays a crucial role in ensuring the safety and stability of structures in these environments.

However, while this study demonstrates the effectiveness of the IDMP in rock instability early warning through laboratory experiments, it is important to note that there are significant differences between laboratory experiments and real-world engineering scales. Due to the small scale of the experiments and relatively simple environmental factors (such as stress distribution, temperature, and humidity), the results from the lab may not fully reflect the complex conditions encountered in actual engineering scenarios. At the engineering scale, variations in rock stress responses and geological conditions may lead to different prediction outcomes than those observed under laboratory conditions. Therefore, scale effects could impact the prediction accuracy of the platform, especially in practical applications like mining, tunnel construction, and landslides in mountainous regions. To further verify the reliability of this decision-making platform in large-scale engineering applications, future research should consider applying the platform in larger-scale experiments or field tests and address prediction errors caused by scale effects. This will not only improve the platform's versatility but also enhance its safety and accuracy in practical applications.

5. Conclusions

1. The fracture network of marble specimens under shear slip is composed of dominant crack and secondary cracks. Dominant cracks have a global scale, the secondary cracks belong to a local scale, and the secondary cracks are distributed around the dominant fractures.
2. Based on LSTM, an IIM of rock shear-slip instability is constructed. LSTM IIM effectively identify the rock shear slip instability and determine the early warning level, and fits recognition effect is good.
3. According to the early warning information, the early warning analysis layer sends out the corresponding early warning signal. The early warning decision-making layer determines the early warning level and makes early warning decisions based on the early warning signals.

Appendix A

Table A1: Input and output layers of marble specimen MRS00-1 (Parts).

	Input layer																Output Layer	
Times (s)	Rise time	Counts	Energy	Duration	Amplitude	Ave. frequency	RMS	ASL	Peak frequency	Threshold	Back-calculated frequency	Initial frequency	Signal intensity	Absolute energy	Center frequency	Peak frequency	1st	2st
4.229718	1	1	1	1	45	1000	0.0006	19	1	45	0	1000	6.28E+03	0.00E+00	115	19	0	0
4.229723	14	2	0	21	45	95	0.0006	20	1	45	142	71	1.80E+03	2.20E+01	112	41	0	0
4.229887	750	23	16	1204	51	19	0.0006	19	13	45	22	17	1.03E+05	1.51E+03	108	45	0	0
4.230107	136	4	2	182	47	22	0.0008	22	2	45	43	14	1.59E+04	2.17E+02	109	41	0	0
4.230181	149	34	26	2100	52	16	0.0006	19	4	45	15	26	1.64E+05	2.08E+03	111	107	0	0
									……									
596.47491	137	115	118	2016	73	57	0.106	63	11	45	55	80	7.41E+05	7.50E+04	138	80	1	0
596.47529	101	142	109	2326	71	61	0.0782	60	10	45	59	99	6.84E+05	5.96E+04	162	92	1	0
596.47548	149	126	94	2292	68	55	0.074	60	13	45	52	87	5.93E+05	4.19E+04	133	81	1	0
596.47510	155	65	38	1508	56	43	0.048	56	9	45	41	58	2.40E+05	6.57E+03	108	40	1	0
596.47541	66	3	0	73	48	41	0.0102	43	3	45	0	45	5.90E+03	8.00E+01	104	84	1	0
									……									
978.20940	4007	995	3870	10,750	99	93	0.1244	64	443	45	81	110	2.42E+07	6.34E+07	155	113	1	1
978.20943	4111	767	2709	11,106	94	69	0.0686	59	339	45	61	82	1.69E+07	1.82E+07	125	45	1	1
978.20955	3891	713	2754	10,645	98	67	0.0766	60	307	45	60	78	1.72E+07	2.45E+07	128	45	1	1
978.20961	3826	578	1384	10,575	90	55	0.034	53	220	45	53	57	8.65E+06	4.82E+06	107	46	1	1
978.20987	220	14	9	642	49	22	0.0014	26	4	45	23	18	5.94E+04	8.46E+02	93	35	0	0

Table A2: Input and output layers of marble specimen MRS20-1 (Parts).

Input layer																	Output layer	
Times (s)	Rise time	Counts	Energy	Duration	Amplitude	Ave. frequency	RMS	ASL	Peak frequency	Threshold	Back-calculated frequency	Initial frequency	Signal intensity	Absolute energy	Center frequency	Peak frequency	1st	2st
0.7896385	2	2	0	33	46	61	0.0006	20	1	45	32	500	3.91E+03	6.17E+01	96	49	0	0
0.861446	1	1	4	1	45	1000	0.001	24	1	45	0	1000	2.52E+04	0.00E+00	138	107	0	0
1.276308	60	21	9	694	49	30	0.001	23	5	45	25	83	5.92E+04	7.98E+02	149	98	0	0
1.276339	21	20	8	675	51	30	0.001	23	3	45	25	142	5.56E+04	7.59E+02	161	98	0	0
1.2763575	76	24	7	432	52	56	0.0008	21	5	45	53	65	4.77E+04	8.36E+02	140	104	0	0
									……									
527.12276	3004	1038	23,275	22,290	99	47	0.3444	73	160	45	45	53	1.45E+08	6.29E+08	131	51	1	0
527.12274	3789	1159	15,848	19,362	99	60	0.2774	71	268	45	57	70	9.90E+07	3.96E+08	161	56	1	0
527.12278	2816	996	21,871	23,918	99	42	0.3344	73	138	45	40	49	1.37E+08	5.88E+08	122	44	1	0
527.12281	2744	1086	23,104	23,464	99	46	0.3508	73	142	45	45	51	1.44E+08	6.43E+08	130	52	1	0
527.12359	1	1	8	1	45	1000	0.008	41	1	45	0	1000	5.62E+04	0.00E+00	112	42	0	0
									……									
1089.5462	16,735	5999	5792	100,001	79	60	0.2814	71	4699	45	73	57	3.62E+07	3.68E+06	120	41	1	1
1089.5469	16,666	8557	5484	100,001	86	86	0.2172	69	6731	45	102	81	3.43E+07	3.94E+06	166	71	1	1
1089.5795	1345	7037	8709	100,001	93	70	0.2712	71	4672	45	71	69	5.44E+07	1.60E+07	68	43	1	1
1089.5935	5	17	7	431	52	39	0.3284	73	1	45	37	200	4.44E+04	7.43E+02	153	83	0	0
1089.5936	255	25	18	1570	49	16	0.1812	68	7	45	13	27	1.19E+05	1.50E+03	118	41	0	0

Table A3: Input and output layers of marble specimen MRS30-1 (Parts).

Input layer																	Output layer	
Times (s)	Rise time	Counts	Energy	Duration	Amplitude	Ave. frequency	RMS	ASL	Peak frequency	Threshold	Back-calculated frequency	Initial frequency	Signal intensity	Absolute energy	Center frequency	Peak frequency	1st	2st
0.8527505	1	1	0	1	45	1000	0.0008	21	1	45	0	1000	4.06E+02	0.00E+00	121	41	0	0
0.8527835	315	3	3	316	48	9	0.0006	20	3	45	0	9	2.09E+04	2.20E+02	128	42	0	0
1.404826	34	2	0	35	46	57	0.0006	19	2	45	0	58	4.05E+03	6.00E+01	89	41	0	0
1.4048535	88	5	2	111	48	45	0.0008	21	4	45	43	45	1.64E+04	3.13E+02	92	44	0	0
1.6192405	307	7	4	464	49	15	0.0008	21	6	45	6	19	3.11E+04	3.48E+02	122	105	0	0
									……								—	—
718.56843	42,664	6892	8092	99,999	93	69	0.2542	71	2819	45	71	66	5.06E+07	2.21E+07	119	98	1	0
718.60484	7	2	0	7	46	286	0.136	65	2	45	0	285	7.02E+02	5.94E+00	153	42	0	0
718.60487	166	7	3	249	52	28	0.0892	62	7	45	0	42	2.16E+04	3.16E+02	130	41	1	0
718.60531	1936	148	90	4948	62	30	0.136	65	53	45	31	27	5.66E+05	1.43E+04	140	41	1	0
718.60575	71	2	0	72	45	28	0.0892	62	2	45	0	28	4.62E+03	4.90E+01	112	41	0	0
									……								—	—
1116.6995	13,309	1696	43,812	34,670	99	49	0.4776	76	738	45	44	55	2.74E+08	1.14E+09	102	61	1	1
1116.6999	13	23	11	509	58	45	0.0048	36	2	45	42	153	7.11E+04	1.71E+03	132	54	0	0
1116.7000	12,992	1558	37,259	31,543	99	49	0.453	76	701	45	46	53	2.33E+08	1.03E+09	115	44	1	1
1116.7001	13,168	1744	36,453	33,665	99	52	0.438	75	825	45	44	62	2.28E+08	9.59E+08	134	46	1	1
1116.7001	81	48	22	964	59	50	0.0052	37	6	45	47	74	1.43E+05	3.69E+03	141	99	0	0

Table A4: Input and output layers of marble specimen MRS50-1 (Parts).

	Input layer																Output layer	
Times (s)	Rise time	Counts	Energy	Duration	Amplitude	Ave. frequency	RMS	ASL	Peak frequency	Threshold	Back-calculated frequency	Initial frequency	Signal intensity	Absolute energy	Center frequency	Peak frequency	1st	2st
0.0077505	997	36	15	2247	56	16	0.0038	35	19	45	13	19	9.77E+04	1.27E+03	220	186	0	0
0.0175735	166	34	16	2414	56	14	0.004	35	2	45	14	12	1.04E+05	1.36E+03	199	114	0	0
0.0273655	447	37	19	2697	55	14	0.004	35	5	45	14	11	1.23E+05	1.69E+03	226	186	0	0
0.0378035	798	32	13	1966	53	16	0.004	35	14	45	15	17	8.35E+04	1.08E+03	213	114	0	0
0.0473455	2246	41	18	2695	52	15	0.004	35	36	45	11	16	1.18E+05	1.45E+03	230	186	0	0
									……								—	—
1846.3984	34,782	4023	7430	55,087	96	73	0.4258	75	2477	45	76	71	4.64E+07	2.03E+07	75	34	1	0
1846.3985	114	24	10	805	51	30	0.1764	67	10	45	20	87	6.68E+04	9.25E+02	132	114	1	0
1846.3998	355	294	166	6195	68	47	0.1764	67	31	45	45	87	1.04E+06	4.11E+04	122	66	1	0
1846.3999	299	30	18	815	56	37	0.034	53	16	45	27	53	1.15E+05	2.68E+03	112	41	1	0
1846.4000	12	6	3	332	48	18	0.0414	55	1	45	15	83	2.48E+04	3.02E+02	104	63	0	0
									……								—	—
2165.7536	4493	300	615	7641	77	39	0.011	43	222	45	24	49	3.84E+06	6.65E+05	81	48	1	1
2165.7537	1	1	0	1	45	1000	0.004	35	1	45	0	1000	0.00E+00	0.00E+00	107	89	0	0
2165.7538	56	1	0	58	47	17	0.0074	40	1	45	0	17	4.36E+03	5.00E+01	94	47	1	1
2165.7542	6	2	0	89	45	22	0.004	35	1	45	12	166	4.75E+03	4.16E+01	89	48	0	0
2165.7544	126	7	5	448	48	16	0.0074	40	2	45	15	15	3.71E+04	4.76E+02	82	48	1	1

Data Availability Statement

The datasets generated and/or analyzed during the current study are available from the corresponding author upon request.

Conflicts of Interest

The authors declare no conflicts of interest.

Author Contributions

Xun You: investigation, formal analysis, data curation, funding acquisition, writing – original draft. **Xiangxin Liu and Yunming Wang:** conceptualization, investigation, supervision, funding acquisition, writing – review and editing. **Kui Zhao and Bin Gong:** methodology, software, resources, writing – review and editing. **Xianxian Liu:** formal analysis, validation.

Funding

The study was funded by the Jiangxi Provincial Natural Science Foundation (Grants 20232ACB214007 and 20232ACG01004), the National Defense Basic Scientific Research Program of China (Grant 2022YFC2904101), and the Royal Society, UK (Grant IES\R2\242319).

Acknowledgments

The authors thank the financial support from the Jiangxi Provincial Natural Science Foundation (Grants 20232ACB214007 and 20232ACG01004), the National Basic Research Program of China (Grant 2022YFC2904101), and the Royal Society, UK (Grant IES\R2\242319).

References

[1] J. Hu, H. Pan, H. Liu, L. Li, H. Fan, and Q. Liu, "Response of Acoustic Emission and Vibration Monitoring Data During Rock Block Collapse in the Tunnel: Small- and Large-Scale Experiments Study," *Tunnelling and Underground Space Technology* 137 (2023): 105121.

[2] Y. Xue, D. Song, J. Chen, et al., "Integrated Rockburst Hazard Estimation Methodology Based on Spatially Smoothed Seismicity Model and Mann-Kendall Trend Test," *International Journal of Rock Mechanics and Mining Sciences* 163 (2023): 105329.

[3] S. Bedaj, "Tunnel, Infrastructure Convergences/Monitoring and Engineering Role," *Engineering* 16, no. 5 (2024): 134–147.

[4] T. Carlà, P. Farina, E. Intrieri, K. Botsialas, and N. Casagli, "On the Monitoring and Early-Warning of Brittle Slope Failures in Hard Rock Masses: Examples From an Open-Pit Mine," *Engineering Geology* 228 (2017): 71–81.

[5] F. Dai, B. Li, N. Xu, and Y. Zhu, "Microseismic Early Warning of Surrounding Rock Mass Deformation in the Underground Powerhouse of the Houziyan Hydropower Station, China," *Tunnelling and Underground Space Technology* 62, no. 2 (2017): 64–74.

[6] Y. Zhao, T. Yang, M. Bohnhoff, et al., "Study of the Rock Mass Failure Process and Mechanisms During the Transformation From Open-Pit to Underground Mining Based on Microseismic Monitoring," *Rock Mechanics and Rock Engineering* 51, no. 5 (2018): 1473–1493.

[7] L.-J. Dong, Z. Tang, X.-B. Li, Y.-C. Chen, and J.-C. Xue, "Discrimination of Mining Microseismic Events and Blasts Using Convolutional Neural Networks and Original Waveform," *Journal of Central South University* 27, no. 10 (2020): 3078–3089.

[8] S. C. Wu, C. X. Zhang, and Z. Q. Cheng, "Rockburst Intensity Classification Prediction Method Based on PCA-PNN Principle," *Journal of China Coal Society* 44, no. 9 (2019): 2767–2776.

[9] X. L. Wu, J. Y. Yang, and R. Q. Niu, "Landslide Susceptibility Evaluation Method Combining SMOTE and Convolutional Neural Network," *Journal of Wuhan University (Information Science Edition)* 45, no. 8 (2020): 1223–1232.

[10] R. Tian, H. D. Meng, S. J. Chen, C. Y. Wang, and F. Zhang, "Rockburst Intensity Classification Prediction Based on Deep Neural Network," *Journal of China Coal Society* 45, no. S1 (2020): 191–201.

[11] C. Liu and Q. Chen, "Deep Learning-Based Multi-Parameter Early Warning Model Under True Triaxial Conditions," *Engineering Geology* 319, no. 6 (2023): 107111.

[12] X.-T. Feng, J. Liu, B. Chen, Y. Xiao, G. Feng, and F. Zhang, "Monitoring, Warning, and Control of Rockburst in Deep Metal Mines," *Engineering* 3, no. 4 (2017): 538–545.

[13] C.-L. Wang, "Identification of Early-Warning Key Point for Rockmass Instability Using Acoustic Emission/Microseismic Activity Monitoring," *International Journal of Rock Mechanics and Mining Sciences* 71, no. 10 (2014): 171–175.

[14] X. M. Zhang, M. H. Wang, D. Feng, and J. C. Wang, "Risk Classification Assessment and Early Warning of Large Deformation of Soft Rock in Tunnels Based on CNN-LSTM Model," *Scientific Report* 14, no. 1 (2024): 29944.

[15] H. Wang, L. Xu, H. Yu, and J. Zhang, "Research on Prediction of High Energy Microseismic Events in Rock Burst Mines Based on BP Neural Network," *Scientific Report* 14, no. 12 (2024): 29934.

[16] F. Huang, H. Xiong, S. H. Jiang, et al., "Modelling Landslide Susceptibility Prediction: A Review and Construction of Semi-Supervised Imbalanced Theory," *Earth-Science Reviews* 250 (2024): 104700.

[17] F. Huang, R. Li, F. Catani, X. Zhou, Z. Zeng, and J. Huang, "Uncertainties in Landslide Susceptibility Prediction: Influence Rule of Different Level of Errors in Landslide Spatial Position," *Journal of Rock Mechanics and Geotechnical Engineering* 16, no. 10 (2024): 4177–4191.

[18] C. Ma, T. Li, H. Zhang, Y. Jiang, and T. Song, "A Method for Numerical Simulation Based on Microseismic Information and the Interpretation of Hard Rock Fracture," *Journal of Applied Geophysics* 164, no. 5 (2019): 214–224.

[19] K. Li, L. Chen, X. Gao, et al., "Implementing Expansion Force-Based Early Warning in LiFePO4 Batteries With Various States of Charge Under Thermal Abuse Scenarios," *Applied Energy* 362 (2024): 122998.

[20] S. Mao, B. Chen, M. Malki, et al., "Efficient Prediction of Hydrogen Storage Performance in Depleted Gas Reservoirs Using Machine Learning," *Applied Energy* 361 (2024): 122914.

[21] X. Liu, L. Wu, Y. Zhang, S. Wang, X. Yao, and X. Wu, "The Characteristics of Crack Existence and Development During Rock Shear Fracturing Evolution," *Bulletin of Engineering Geology and the Environment* 80, no. 2 (2021): 1671–1682.

[22] T. Fischer and C. Krauss, "Deep Learning With Long Short-Term Memory Networks for Financial Market Predictions," *European Journal of Operational Research* 270, no. 2 (2018): 654–669.

[23] T. N. Sainath, O. Vinyals, A. Senior, and H. Sak, "Convolutional, Long Short-Term Memory, Fully Connected Deep Neural Networks," in *2015 IEEE International Conference on Acoustics, Speech and Signal Processing (ICASSP)*, (South Brisbane, QLD, Australia: IEEE, 2015), 4580–4584.
[24] C. Li, Z. Wang, M. Rao, et al., "Long Short-Term Memory Networks in Memristor Crossbar Arrays," *Nature Machine Intelligence* 1, no. 1 (2019): 49–57.
[25] R. E. Goodman, "Subaudible Noise During Compression of Rocks," *Geological Society of America Bulletin* 74, no. 4 (1963): 487–490.
[26] Y. B. Zhang, P. Liang, X. X. Liu, S. J. Liu, and B. Z. Tian, "Experimental Study on Precursor of Rock Fracture Based on Main Frequency and Entropy Value of Acoustic Emission Signals," *Chinese Journal of Rock Mechanics and Engineering* 34, no. S1 (2015): 2959–2967.
[27] X. X. Liu, Y. B. Zhang, Z. Z. Liang, and S. J. Liu, "Study on Information Recognition of Acoustic Emission Monitoring Frequency Band for Rock Fracture Instability," *Chinese Journal of Geotechnical Engineering* 39, no. 6 (2017): 1096–1105.
[28] F. Zhao, S. Z. Meng, D. Q. Liu, et al., "Study on Precursor Information of Granite Rockburst Failure Based on Acoustic Emission Signal Characteristics," *Chinese Journal of Rock Mechanics and Engineering* 43, no. 11 (2024): 2669–2686.
[29] H. G. Ji, C. R. Zhang, Y. Z. Zhang, et al., "Study on Stress State and Energy Evolution of Acoustic Emission Signals During Fracture Process of Rock Materials," *Journal of China University of Mining and Technology* 53, no. 2 (2024): 211–223.
[30] R. Axel and M. Rafael, "Performance Evaluation of Hydrological Models: Statistical Significance for Reducing Subjectivity in Goodness-of-Fit Assessments," *Journal of Hydrology* 480, no. 1 (2013): 33–45.
[31] J. Xiao, G. Sun, C. Song, D. Wang, and X. Lin, "Security Monitoring, Early Warning and Alarm Method Based on Security Boundary for Regional Integrated Energy System," *Applied Energy* 379 (2025): 124709.